Reaction Chemistry & Engineering

ROYAL SOCIETY OF CHEMISTRY

PAPER

View Article Online
View Journal

Cite this: DOI: 10.1039/d6re00079g

WO_3-modified KIT-6 catalysts synthesized *via* a non-hydrolytic sol–gel method for glycerol dehydration to acrolein

Busra Kaya,*[a] Mohammed Alfatih Hamid,*[b] Yasar Zengin,[a] Mehtap Safak Boroglu[a] and Ismail Boz[c]

Received 8th March 2026,
Accepted 21st April 2026

DOI: 10.1039/d6re00079g

rsc.li/reaction-engineering

The expansion of biodiesel production has generated a surplus of glycerol. The valorization of this renewable by-product into value-added chemicals has therefore gained increasing interest. This study presents a systematic investigation of WO_3/KIT-6 catalysts prepared *via* a non-hydrolytic sol–gel (NHSG) method for glycerol dehydration to acrolein. Catalysts with 5–35 wt% WO_3 were synthesized and systematically characterized. XRD confirms the formation of monoclinic WO_3 across the investigated samples. The 25 wt% WO_3/KIT-6 catalyst exhibits the highest medium-strength acid site concentration (204 μmol NH_3 per g), intrinsic acidity (0.56 μmol NH_3 per m^2), and a Brønsted/(Brønsted + Lewis) ratio of 0.67. Under the studied reaction conditions, this catalyst achieves 83% glycerol conversion and 43% acrolein selectivity. The results indicate that an optimal balance between medium-strength acidity and mesostructural properties governs acrolein selectivity and catalyst stability.

1. Introduction

The rapid expansion of biodiesel production has led to a surplus of glycerol, the primary by-product formed at a mass ratio of approximately 1 : 10 relative to biodiesel.[1] Glycerol is a renewable carbon source with clear environmental advantages over conventional petrochemical feedstocks. Acrolein is a valuable intermediate for the production of esters, acrylic acid, and polymers. It is conventionally manufactured by gas-phase oxidation of propylene over Bi/Mo oxide catalysts at 300–400 °C, with reported yields of 70–80%. A more sustainable route involves vapor-phase dehydration of glycerol over solid acid catalysts. The efficiency of this process depends strongly on acid strength and the nature of the active sites.[2–4] Mechanistically, glycerol dehydration proceeds through the formation of 3-hydroxypropanal as a key intermediate, which subsequently converts to acrolein.[5]

WO_3 is an established solid acid catalyst with tunable acidity, redox properties, and structural stability.[6,7] Several synthetic routes, including impregnation,[8] solvothermal methods,[9] and surfactant-assisted techniques,[10,11] have been employed to prepare WO_3-based catalysts. The preparation method strongly influences active phase dispersion, crystal growth, and metal–support interactions.[12] The non-hydrolytic sol–gel (NHSG) method provides control over condensation reactions during oxide formation in non-aqueous media. In contrast to conventional sol–gel routes, NHSG employs organic oxygen donors such as ethers, carboxylates, and alcohols. This approach improves compositional homogeneity and structural stability.[13] Interest in NHSG-derived WO_3 catalysts has therefore increased.[14,15]

Previous studies have demonstrated the advantages of NHSG-synthesized WO_3/SiO_2 catalysts. These systems exhibit high acidity and promising catalytic performance in reactions such as ethene cross-metathesis[16] and glycerol dehydration.[17] WO_3 has also been supported on silica-based materials such as MCM-48 (ref. 18) and SBA-15,[19] as well as on metal oxides such as Al_2O_3.[8] Supported WO_3 catalysts generally display high surface area and mesoporosity, which influence catalytic performance.[20]

The catalytic performance of WO_3-based materials is strongly influenced by the chemical nature of the support. Different oxide supports such as Al_2O_3, TiO_2, and ZrO_2 have been widely studied, showing that the support affects tungsten dispersion, surface species, and acidity. In particular, WO_3/TiO_2 systems exhibit a relationship between WO_3 surface coverage, the formation of mono- and polytungstate species, and the development of Brønsted acidity, which impacts acrolein formation.[21] Similarly, WO_3/ZrO_2 catalysts demonstrate that the interaction between tungsten oxide and the support governs the type and strength of acid sites, as well as catalytic selectivity.[22,23] At

[a] *Faculty of Engineering, Chemical Engineering Department, Istanbul University-Cerrahpaşa, Avcilar, 34320 Istanbul, Turkey*
[b] *Faculty of Science, Department of Chemistry, Bilkent University, Cankaya, 06800 Ankara, Turkey. E-mail: alfatiham874@gmail.com*
[c] *Bandirma Onyedi Eylul University, Rectorate, Merkez Yerleskesi, Bandirma, 10200 Balikesir, Turkey*

low WO_3 loading, isolated species dominate, while increasing loading leads to polymeric WO_x species and eventually crystalline WO_3, which may reduce the number of active sites. Therefore, understanding the role of the support is essential for optimizing catalyst design.

Among the available supports, KIT-6 is a mesoporous silica material with a three-dimensional pore architecture and tunable pore diameters in the 4–12 nm range.[24–26] It possesses a high surface area (600–800 $m^2\ g^{-1}$) and interconnected channels that facilitate mass transport and active site accessibility.[27] KIT-6-supported NbW catalysts have shown higher acrolein yields than unsupported systems.[2,28] The thick pore walls and hydrolytic stability of KIT-6 help preserve structural integrity under reaction conditions.[29,30]

Despite these advances, NHSG-derived WO_3/KIT-6 catalysts have not been systematically evaluated for glycerol dehydration to acrolein. This study examines the effect of WO_3 loading on structural properties, acidity, and catalytic performance. The relationship between surface acidity parameters and acrolein selectivity is analyzed. Particular attention is given to the distribution and strength of acid sites and their influence on catalytic behavior.

2. Experimental section

2.1. Reagents and materials

Dichloromethane (≥99.8%), diisopropyl ether (≥99.5%), hydrochloric acid (HCl, 35%), and pluronic P123 triblock copolymer were purchased from Sigma-Aldrich. Tungsten(VI) chloride (WCl_6, 99%) was obtained from Alfa Aesar. *n*-Butanol (≥99%) and tetraethyl orthosilicate (TEOS, 98%) were supplied by Merck. All chemicals were used as received without further purification.

2.2. Synthesis of the KIT-6 support

The KIT-6 silica support was synthesized as follows: 9.8 g of hydrochloric acid was dissolved in 181 g of deionized water and the mixture was agitated for 5 min. Pluronic P123 (5 g) was subsequently introduced, and the resulting solution was kept under stirring at 35 °C for 6 h until a homogeneous mixture was achieved. Thereafter, 5 g of *n*-butanol and 10.1 g of tetraethyl orthosilicate (TEOS) were added dropwise over the course of 1 h at 35 °C. The mixture was allowed to continue stirring at 35 °C for an additional 24 h. The resulting gel was then carefully transferred into a Teflon-lined autoclave and subjected to hydrothermal crystallization at 120 °C for 24 h. Following hydrothermal treatment, the solid product was recovered and dried at 80 °C for 12 h. The dried material was subsequently calcined in a static air atmosphere at 550 °C for 6 h, applying a controlled heating rate of 1 °C min^{-1}.[18]

2.3. Preparation of WO_3/KIT-6 catalysts

The catalysts are denoted as *x*W–KIT-6, where *x* indicates the nominal tungsten content (5, 15, 25, or 35 wt%), adjusted by varying the amount of WCl_6. The NHSG synthesis employed WCl_6, diisopropyl ether, and dichloromethane as reagents, with a diisopropyl ether-to-WCl_6 molar ratio of 1 : 1. All handling was performed in a glove box maintained below 1% moisture. KIT-6, WCl_6, and diisopropyl ether were combined, and 20 mL of dichloromethane was introduced dropwise under agitation. After stirring for 10 min, the slurry was transferred to a Teflon-lined autoclave and heated at 120 °C for 24 h. Upon cooling, the recovered solid was washed three times with dichloromethane, dried under vacuum at 100 °C in a nitrogen atmosphere for 12 h, and subsequently calcined in air at 500 °C for 3 h at a ramp rate of 3 °C min^{-1}.[17]

2.4. Catalyst characterization techniques

XRD patterns were collected on a Rigaku D/Max-2200 diffractometer (Cu Kα, λ = 1.54059 Å) over a 2θ range of 10–50° at 40 kV, 30 mA, and a scan rate of 2° min^{-1}. Textural properties (BET surface area, pore volume, and pore size distribution) were determined from N_2 adsorption–desorption isotherms recorded on a TriStar II 3020 instrument; samples (~0.3 g) were degassed at 200 °C for 4 h prior to measurement. Brønsted and Lewis acid sites were probed by pyridine adsorption DRIFTS using a Thermo Nicolet 380 spectrometer; pellets of the catalysts (0.01 g) and KBr (0.2 g) were activated under vacuum at 400 °C for 1 h, exposed to 5 μL pyridine at room temperature, and then heated to 150 °C before spectral collection. SEM imaging was conducted on a Zeiss Ultra Plus microscope (SE2 detector, 5.0 kV, working distance 5.0–5.1 mm). XPS measurements were performed on a Thermo Scientific K-Alpha spectrometer (Al Kα, 1486.3 eV), with binding energies referenced to the C 1s peak at 284.5 eV and spectra processed using Avantage 5.9 software. Raman spectra were acquired on a Bruker spectrometer with a 532 nm laser. Surface acidity was quantified by NH_3-TPD on a ChemBet-3000 system coupled to an Agilent 5973 mass spectrometer; ~0.2 g of sample was pretreated in static air at 400 °C for 6 h, then exposed to 5 wt% NH_3/He (80 mL min^{-1}) at 100 °C for 25 min. After physisorbed NH_3 removal by He purging (80 mL min^{-1}, 60 min, 100 °C), desorption was carried out from 100 to 600 °C at 10 °C min^{-1} under an 80 mL min^{-1} He flow. ICP-MS measurements were conducted using an Agilent 7700 Series X spectrometer featuring a third-generation Octopole Reaction System (ORS3) with helium as the collision/reaction gas.

2.5. Catalytic reaction setup

Catalytic dehydration of glycerol was carried out in a stainless steel fixed-bed tubular reactor with an inner diameter of 7.5 mm. The catalyst was mixed with quartz particles prior to being packed into the reactor. All experiments were carried out at 300 °C under ambient pressure conditions. The reactor setup comprised dual PID-regulated heating zones, Brooks 5850 TR mass flow controllers, a Reaxus HPLC pump for continuous liquid delivery, and a downstream condenser for product recovery. The catalyst underwent a pretreatment step under a nitrogen atmosphere at 300 °C for 30 min. A 10 wt%

glycerol solution in water was fed into the reactor at a volumetric flow rate of 7.2 mL h^{-1}. A mixed gas stream consisting of 20% O_2 balanced in N_2 was delivered at a flow rate of 45 mL min^{-1}. Condensed liquid products were recovered and analyzed using an Agilent 6890N gas chromatograph equipped with an autosampler, a flame ionization detector (FID), and an INNOWAX capillary column (30 m × 0.32 mm × 0.50 μm). The injector temperature was maintained at 250 °C, and 1 μL samples were injected in split mode (10 : 1). The oven temperature program was as follows: an initial temperature of 35 °C held for 5 min, ramped at 5 °C min^{-1} to 90 °C, then increased at 10 °C min^{-1} to 150 °C, and finally increased at 20 °C min^{-1} to 300 °C, where it was held for 12 min. The FID temperature was maintained at 280 °C. Hydrogen and air flow rates were 35 and 350 mL min^{-1}, respectively, while nitrogen was used as make-up gas at 25 mL min^{-1}. Prior to analysis, liquid samples were cooled to room temperature and filtered. For quantitative analysis, 1 mL of each sample was combined with 0.1 mL of *n*-butanol as an internal standard. Reaction products were identified and quantified using calibration curves based on the internal standard method.

The following mathematical expressions were used to determine glycerol conversion (x), product selectivity (S_{Prod}), and product yield (Y_{Prod}). $n_{Gly,in}$ and $n_{Gly,out}$ denote the molar flow rates of glycerol at the reactor inlet and outlet, respectively. n_{prod} represents the molar amount of each product. Z_{prod} and Z_{Gly} correspond to the number of carbon atoms in the product and glycerol, respectively. The overall carbon balance was calculated based on the contributions of all quantified products in the condensed effluent.

$$x(\%) = \frac{n_{Gly,in} - n_{Gly,out}}{n_{Gly,in}} \times 100$$

$$S_{Prod}\ (\%) = \frac{Z_{prod} \cdot n_{prod}}{Z_{Gly} \cdot \left(n_{Gly,in} - n_{Gly,out}\right)} \times 100$$

$$Y_{Prod}\ (\%) = \frac{x \times S_{Prod}}{100}$$

3. Catalyst characterization

3.1. Crystallinity and structural analysis

Fig. 1 presents the low-angle XRD pattern of the synthesized KIT-6 support (0.5–2° 2θ range). Distinct reflections are observed at 2θ = 1.03°, 1.10°, and 1.76°, which are indexed to the (211), (220), and (332) planes, respectively. These reflections are characteristic of a three-dimensional cubic mesostructure with the *Ia3d* symmetry, consistent with reported KIT-6 materials.[27] The presence of the (211) reflection indicates well-defined mesoscopic ordering within the silica framework. The observed diffraction features indicate the formation of an ordered mesoporous structure prior to WO_3 loading.[31,32]

Fig. 2 presents the wide-angle XRD patterns of W–KIT-6 catalysts with tungsten loadings ranging from 0 to 35 wt%.

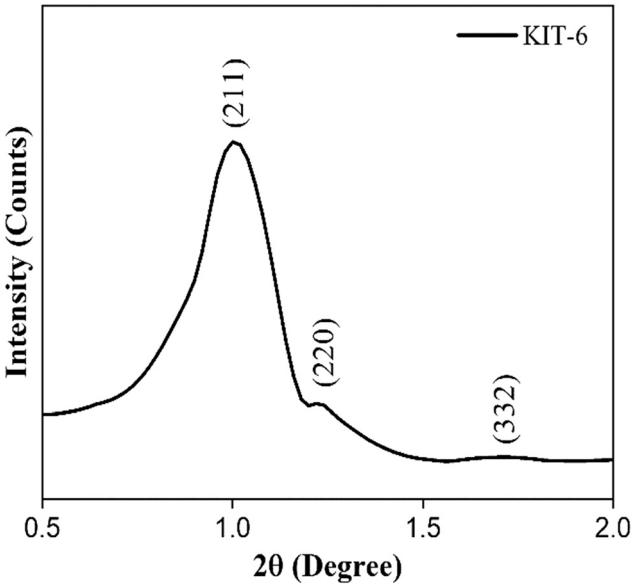

Fig. 1 XRD diffractogram of the pristine KIT-6 silica support.

Diffraction peaks at 2θ = 23.1°, 23.5°, and 24.3° are assigned to the (002), (020), and (200) planes of monoclinic WO_3 (JCPDS no. 83-0950).[33] For loadings of 15 wt% and higher, sharp and well-defined reflections are observed, indicating the formation of a crystalline WO_3 phase. In contrast, the 5 wt% sample exhibits weak and broadened features, which may be associated with smaller crystallite size or more dispersion of tungsten oxide. The intensity of the monoclinic WO_3 reflections increases with tungsten loading.

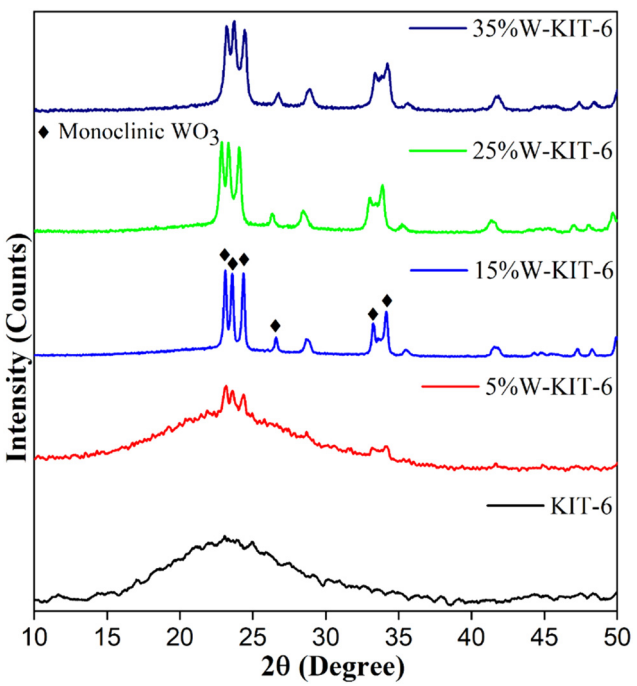

Fig. 2 XRD diffractograms of W–KIT-6 catalysts at varying tungsten contents (wt%).

This trend indicates progressive development of the crystalline phase. No additional crystalline impurity phases were detected within the measured range. In addition to the WO_3 reflections, a broad diffuse feature centered around $2\theta \approx 15–30°$ can be attributed to the amorphous silica framework of KIT-6.[34] Due to its non-crystalline nature, silica does not produce sharp diffraction peaks, and its contribution appears as a low-intensity halo in the diffraction pattern. The dominance of WO_3 reflections, particularly at higher loadings, may further obscure this broad feature.

3.2. Textural properties and surface area analysis

The nitrogen adsorption–desorption isotherms of KIT-6 and W–KIT-6 catalysts (Fig. 3) exhibit type IV behavior with a hysteresis loop in the relative pressure (P/P^0) range of 0.6–0.8, characteristic of mesoporous materials according to the IUPAC classification.[27,35] These features indicate the presence of a mesoporous structure in both the parent support and W-loaded samples. Similar type IV isotherms have been reported for metal-loaded mesoporous silicas, including Fe/SBA-15 systems. These observations suggest preservation of mesoporosity after metal incorporation.[36]

The pure KIT-6 support displays a surface area of 719 $m^2\ g^{-1}$ and an average pore diameter of 7.0 nm, consistent with reported values for KIT-6.[31] Upon loading of WO_3, the BET surface area decreases progressively with increasing W loading. The surface area decreases from 424 $m^2\ g^{-1}$ for 5 wt% W–KIT-6 to 355 $m^2\ g^{-1}$ for 35 wt% W–KIT-6 (Table 1). This reduction may be associated with the presence of tungsten oxide species dispersed on the surface and possibly within the mesoporous channels. The pore size distributions remain within the mesoporous range, indicating retention of the overall pore structure after WO_3 loading. Similar observations have been reported for metal-loaded KIT-6

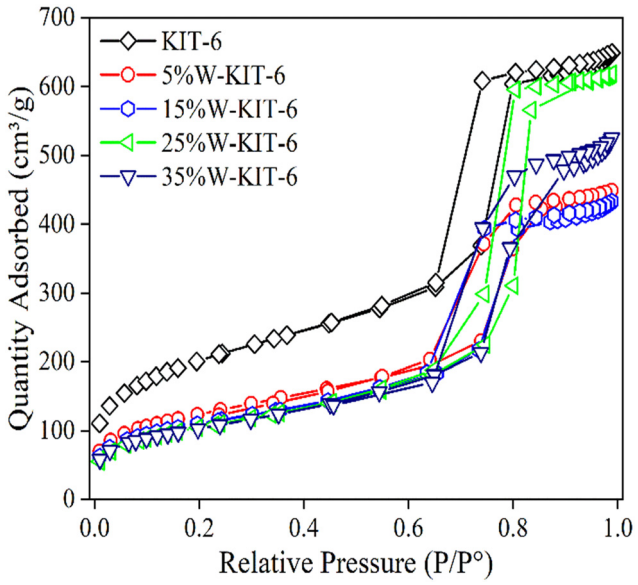

Fig. 3 Nitrogen adsorption–desorption isotherms.

Table 1 Physicochemical properties of KIT-6-based catalysts synthesized *via* the NHSG route and their catalytic activity in the dehydration of glycerol

Catalyst	ICP-MS (wt%)	Surface area, $m^2\ g^{-1}$	Av. pore size (nm)	B/(B + L), FTIR (pyridine)	NH_3-TPD (μmol NH_3 per g)				Medium acidity/area (μmol NH_3 per m^2)	Conv. (%)	ACA sel. (%)	ACR sel. (%)	Other	Condensable product (%)	ACR yield (%)
					Weak	Medium	Strong	Total							
KIT-6	nd	719	7.0	0	nd	nd	nd	nd	nd	46	4	4	0	10	2
5% W–KIT-6	3.78	424	6.1	0.30	130	66	9	205	0.156	78	6	23	5	34	18
15% W–KIT-6	14.11	382	6.4	0.48	181	174	102	457	0.455	82	9	28	3	40	23
25% W–KIT-6	23.50	376	7.8	0.67	232	204	40	476	0.561	83	10	43	6	59	36
35% W–KIT-6	33.70	355	8.1	0.18	153	180	65	398	0.507	81	8	34	4	56	28

Data obtained at 2 h on stream under the following operating conditions: 0.97 *g* catalyst, 300 °C reaction temperature, 45 mL h^{-1} of 20% O_2/N_2 feed, W/F ratio of 110 g_{cat} h mol_{GLY}^{-1}, 10 wt% aqueous glycerol feed at 7.34 g h^{-1}. ACR: acrolein; ACA: acetaldehyde; others: acetol, propanal, allyl alcohol, and propionic acid; nd: not determined.

systems.[31,37] The textural data indicate that tungsten loading influences the surface area and pore characteristics while maintaining mesoporous features within the investigated loading range. The mesoporous KIT-6 structure is largely preserved after WO_3 loading, as indicated by the retention of type IV isotherms and mesoporous pore size distribution.

3.3. Acidity and acid site distribution

The absorption band centered at approximately 3452 cm^{-1} in Fig. 4(a) is assigned to the O–H stretching vibrations of surface silanol (Si–OH) groups.[38] The band near 1629 cm^{-1} corresponds to the bending vibration of adsorbed water molecules interacting with these hydroxyl groups.[39] The bands at 793, 1053, and 1252 cm^{-1} are attributed to the symmetric and asymmetric stretching modes of Si–O–Si bonds within the silica framework.[40] The bands at 949 and 459 cm^{-1} are associated with the Si–O stretching vibrations related to silanol groups and framework oxygen linkages.[41,42] These features indicate the presence of surface hydroxyl sites and are consistent with preservation of the silica network structure.

The synthesis parameters used in the preparation of KIT-6 influence the organization of the silica framework and the distribution of hydroxyl groups.[43,44] Template concentration, alcohol type, and aging time affect pore architecture and silanol interactions. Changes in these parameters can modify the intensity and position of vibrational bands. Previous studies have shown that variations in aging time or alcohol selection may result in the formation of hexagonal SBA-15 instead of cubic KIT-6.[45,46] Such structural transitions alter the Si–O–Si framework. In the present study, no additional bands corresponding to alternative silica phases were detected. The spectral features are consistent with the preservation of the cubic KIT-6 structure under the applied synthesis conditions.

Brønsted (B) and Lewis (L) acid sites were differentiated by pyridine adsorption infrared spectroscopy, where absorption bands at 1540 cm^{-1} and 1450 cm^{-1} are characteristic of Brønsted and Lewis acidity, respectively.[47] The B/(B + L) ratio was calculated from the relative integrated areas of these bands. The Brønsted acidity values and corresponding B/(B + L) ratios were 31.48 μmol g^{-1} and 0.30 for 5 wt% W–KIT-6, 89.01 μmol g^{-1} and 0.48 for 15 wt%, 150.89 μmol g^{-1} and 0.67 for 25 wt%, and 18.45 μmol g^{-1} and 0.18 for 35 wt%. The highest Brønsted acidity was observed for the 25 wt% catalyst. The synthesis method influences both the total acidity and the distribution of Brønsted and Lewis acid sites.[48] The corresponding B/(B + L) ratios are listed in Table 1 and presented in Fig. 4(b). The variation of Brønsted and Lewis acidity with tungsten loading follows a trend comparable to that reported by Aihara *et al.*[8] In that study, the maximum Brønsted acidity (~45 μmol g^{-1}) was obtained for a 20 wt% WO_3/Al_2O_3 catalyst.

In the present system, Brønsted acidity increases from 5 to 25 wt% and decreases at 35 wt%. The NHSG-derived catalysts exhibit higher Brønsted acidity than catalysts prepared by impregnation at comparable tungsten loadings.[49,50] This difference may be associated with the formation of additional surface WO_x species, including W–OH groups and polymeric WO_x domains. At higher tungsten loadings, the contribution of polymeric WO_x species is expected to become more significant, consistent with literature reports on supported tungsten oxides.[51,52]

NH_3-TPD was utilized to assess the total surface acidity and acid strength distribution across all catalysts. Based on the NH_3 desorption temperature, acid sites were classified into three categories: weak (100–250 °C), medium (250–400 °C), and

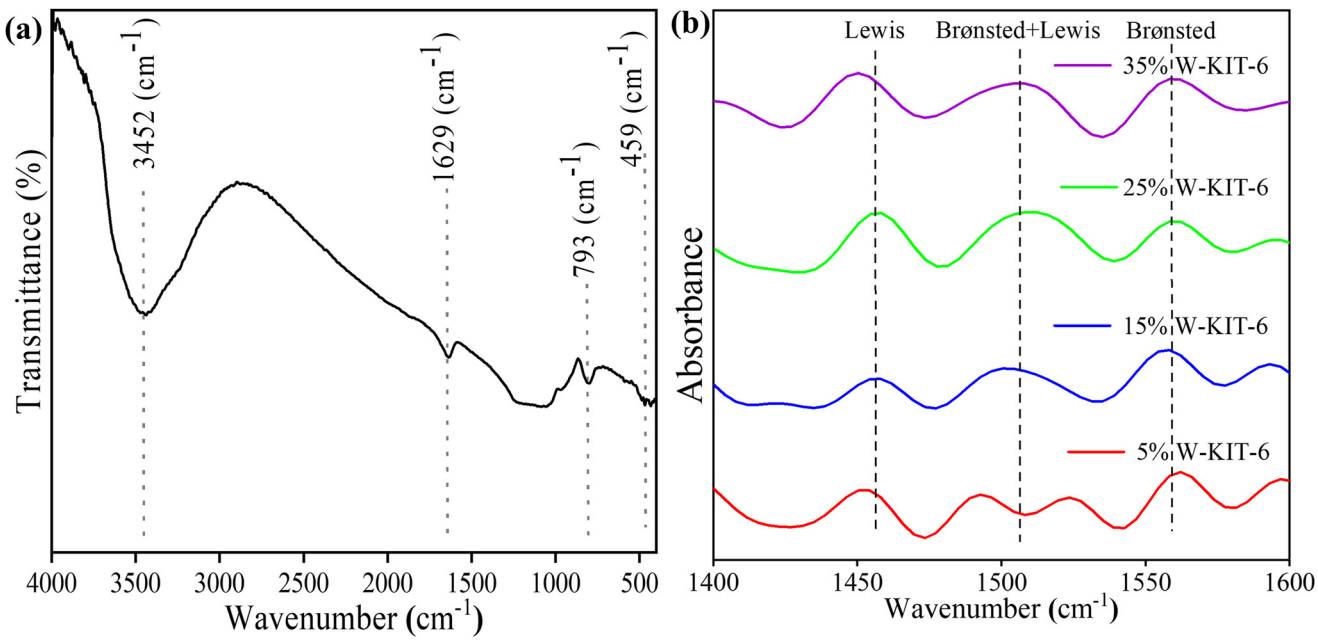

Fig. 4 (a) FTIR pattern of pure KIT-6. (b) FTIR-pyridine patterns of W–KIT-6 catalysts with varying wt% loadings.

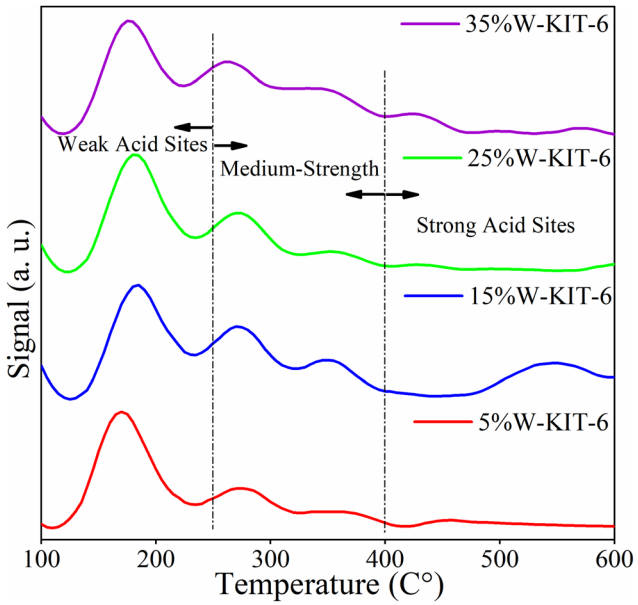

Fig. 5 NH_3-TPD profiles of W–KIT-6 catalysts (5–35 wt% W). Acid site regions are classified as weak (100–250 °C), medium (250–400 °C), and strong (400–600 °C).

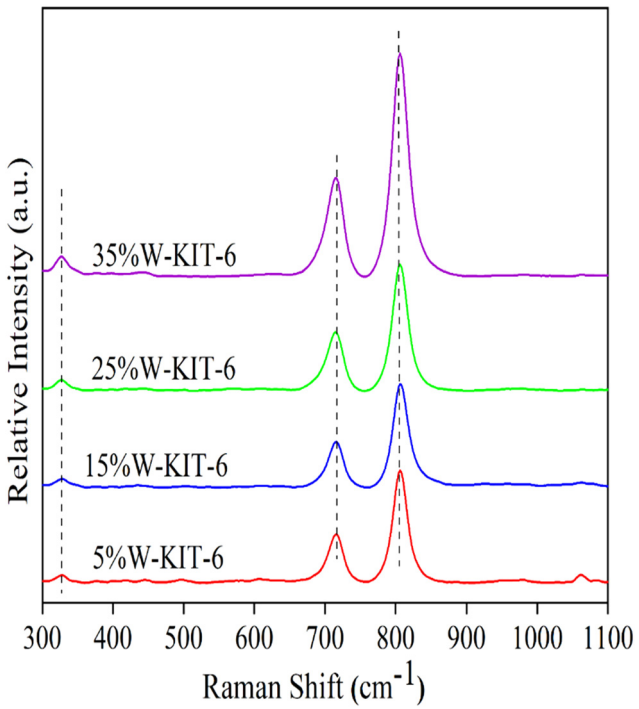

Fig. 6 Raman spectra of KIT-6 catalysts loaded with varying wt% of W.

strong (400–600 °C). The resulting TPD profiles are shown in Fig. 5, while the associated quantitative data are provided in Table 1. Total acidity increases with W loading on KIT-6, rising from 205 to 476 μmol NH_3 per g as the W content increased from 5% to 25%. Medium acid sites showed a consistent increase with tungsten content, yielding 66, 174, and 204 μmol NH_3 per g for 5%, 15%, and 25% W loadings, respectively. Strong and weak acid sites exhibited different trends, reaching optimal values at 15% and 25% W loadings, respectively.

The NHSG synthesis method employed in this study yielded catalysts with higher acidity compared to similar catalysts prepared by alternative methods. For equivalent W loadings, catalysts prepared *via* wet impregnation (Poovarawan *et al.*, 2015) and sol–gel methods (Kulal *et al.*, 2016) showed total acidities of 152 and 140 μmol NH_3 per g, respectively, compared to 205 μmol NH_3 per g achieved in this work.[49,50] Similarly, Wu *et al.* reported a total acidity of 200 μmol NH_3 per g for 13% W–KIT-6 prepared by a one-pot method, whereas our 15% W–KIT-6 exhibited significantly higher acidity (457 μmol NH_3 per g).[53] This enhanced acidity may be associated with a more uniform distribution of WO_x species generated by the NHSG method.

3.4. WO_3 phase dispersion and catalyst interaction

The Raman spectra of the W–KIT-6 catalysts are presented in Fig. 6. The spectra show characteristic bands at approximately 324, 711, and 807 cm^{-1}. These bands correspond to the O–W–O bending and stretching vibrations of monoclinic WO_3.[54] The intensity of these bands increases with tungsten loading. This indicates the progressive formation of crystalline WO_3 domains at higher W contents. The bands at 5% and 15% W are broader than those at 25% and 35% W. The sharper peaks at 35% W indicate the growth of more crystalline WO_3 domains. No significant shift in the peak position is observed with increasing WO_3 loading.

The monoclinic phase is therefore retained across all compositions. The characteristic Si–O–Si framework vibrations of KIT-6 are not clearly resolved in the W-containing samples. The strong WO_3 band near 800 cm^{-1} overlaps with the silica stretching region. The silica Raman signal may also be attenuated due to progressive surface coverage by WO_x species. This behavior suggests an increasing metal–support interaction with higher tungsten loading. The NHSG synthesis route may promote a more uniform distribution of WO_x species and enhanced contact with the silica framework.

The SEM micrographs of the 25 wt% W–KIT-6 catalyst are presented in Fig. 7(a and b). The images reveal aggregated particles with irregular morphology typical of silica-based materials synthesized *via* NHSG.[55] Bright contrast domains are observed and may be attributed to WO_3-rich regions. These domains appear distributed across the surface without evidence of large bulk crystallites. SEM does not provide direct information about mesopore ordering or the location of WO_3 species within the KIT-6 framework. Therefore, conclusions regarding internal *versus* external deposition cannot be drawn solely from these images.

For comparison, the SEM images of pure KIT-6 are presented in Fig. S1 to illustrate the overall morphological features prior to W incorporation.

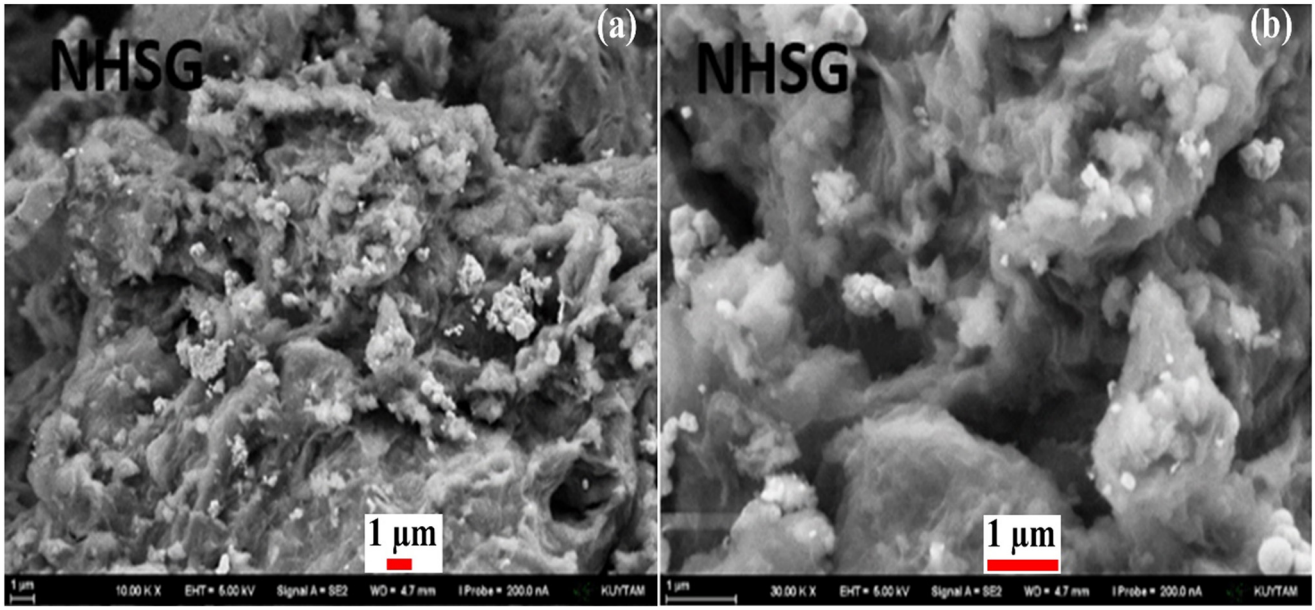

Fig. 7 SEM micrographs of the 25% W–KIT-6 catalyst: (a) and (b) show representative morphology of the sample.

XPS analysis of the 25% W–KIT-6 catalyst was performed to determine the surface composition and oxidation states of tungsten oxide species. The survey spectrum is presented in Fig. S2. The Si 2p spectrum (Fig. S3) exhibits two components at 101.78 eV and 104.21 eV, which are characteristic of Si^{4+} species in a silica framework.[56,57] These binding energies confirm that the mesoporous KIT-6 structure remains intact after WO_3 deposition on the support. The W 4f region (Fig. S3) shows two deconvoluted peaks at 33.78 eV and 35.95 eV, assigned to W^{6+} and W^{5+} species, respectively.[58] The presence of W^{5+} indicates partial surface reduction of tungsten species associated with oxygen-deficient WO_{3-x} environments. Such reduced sites may arise from oxygen vacancies, the high dispersion of surface WO_x domains, and residual organic species decomposed during calcination of the NHSG-derived gel.[17] In addition, the relatively weak interaction between tungsten oxide species and the silica support may further favor stabilization of partially reduced surface tungsten centers. Thus, the coexistence of W^{6+}/W^{5+} species reflects surface heterogeneity rather than bulk reduction of WO_3.

The O 1s spectrum (Fig. S2) reveals two oxygen environments. The dominant peak at 531.40 eV corresponds to lattice oxygen in WO_3. The lower binding energy component at 528.33 eV is attributed to oxygen associated with reduced WO_{3-x} species (Table S1).[59] The higher proportion of lattice oxygen relative to reduced oxygen species indicates that fully oxidized WO_3 is the predominant surface phase. The coexistence of W^{6+}/W^{5+} species and WO_3/WO_{3-x} oxygen environments reflects surface heterogeneity and defect sites. These features may be associated with the formation of acid sites related to tungsten oxide domains.

4. Catalytic performance

The catalytic performance of KIT-6-supported WO_3 catalysts in glycerol dehydration depends on tungsten loading, surface acidity, and pore structure. Acrolein selectivity varies with changes in WO_3 content and acid site distribution. The influence of WO_3 loading on product distribution is first evaluated. The relationship between Brønsted and Lewis acid sites and catalytic behavior is then examined. The effect of pore structure on diffusion, selectivity, and stability is subsequently analyzed. These parameters are assessed to identify conditions that favor acrolein formation while limiting by-product formation and catalyst deactivation.

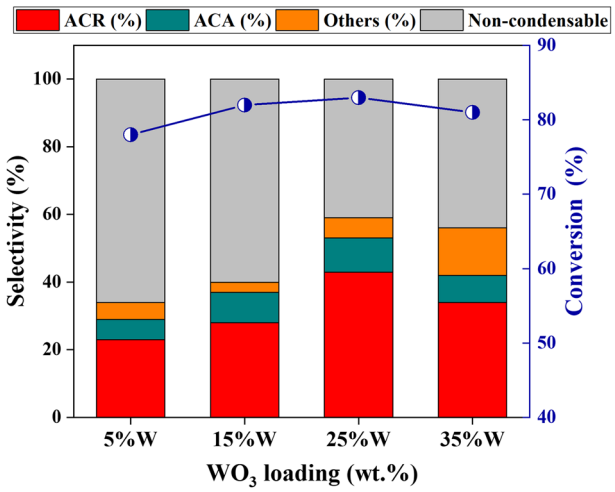

Fig. 8 Effect of tungsten loading (5–35 wt%) on glycerol conversion and acrolein selectivity over W–KIT-6 catalysts.

4.1. Effect of WO_3 loading on acrolein selectivity

As shown in Fig. 8, acrolein selectivity increases with W loading up to 25% W–KIT-6 and reaches a maximum value of 43%. This result indicates that tungsten content influences acrolein formation. Acetaldehyde is detected as a secondary product for all catalysts. Its selectivity is 6%, 9%, 10%, and 8% for 5%, 15%, 25%, and 35% W–KIT-6, respectively. The increase in acrolein selectivity up to 25% W suggests that moderate WO_3 loading enhances the desired dehydration pathway. At 35% W, the slight decrease in acrolein selectivity may indicate the contribution of competing reactions. These results show that catalytic performance depends on WO_3 loading within the investigated range.

4.2. Acid strength and site ratios in acrolein production

The effect of Brønsted acidity on acrolein yield has been previously reported by Cecilia *et al.*,[19] who demonstrated that the optimal acrolein production is achieved at an optimal concentration of Brønsted acid sites. This aligns with our findings, where maximum acrolein selectivity was observed with intermediate W loading, specifically in the 25% W–KIT-6 catalyst. This catalyst not only provides a balanced density of Brønsted acid sites, but also falls within the ideal W content range (20–30% WO_3 on the support), which has been shown to enhance acrolein formation by promoting efficient dehydration pathways while minimizing side reactions.

Nadji *et al.*[17] examined the effect of the Brønsted/(Brønsted + Lewis) ratio in WO_3/SiO_2 and WO_3–ZrO_2/SiO_2 systems. Their results indicate that W and Zr loading influence acid site distribution and acrolein selectivity. In the present work, both the B/(B + L) ratio and the concentration of medium-strength acid sites show a correlation with acrolein yield, as illustrated in Fig. 9. This observation suggests that acid site balance may contribute to the selective formation of acrolein under the studied conditions.

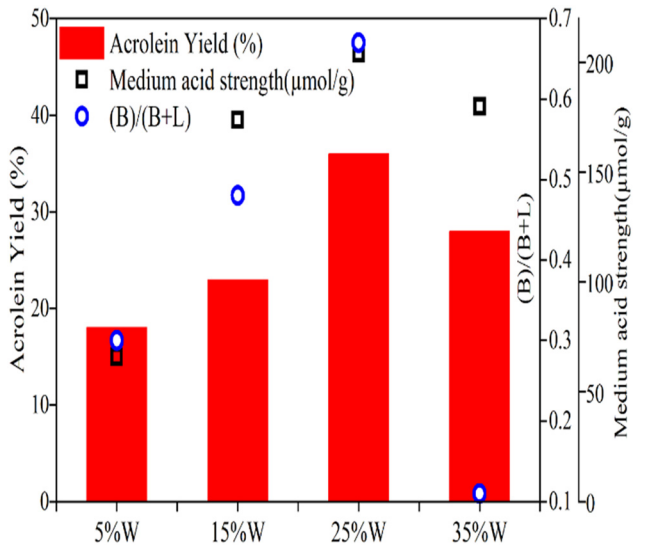

Fig. 9 Relationship between acrolein yield, medium-strength acid site concentration, and B/(B + L) ratio.

Among the investigated catalysts, the 25% W–KIT-6 sample demonstrates a notably elevated medium-strength acid site concentration (204 μmol NH_3 per g) alongside a balanced B/(B + L) ratio. This catalyst shows the highest acrolein yield (36%) under the studied conditions. The correlation between acrolein yield, medium acid strength, and B/(B + L) ratio suggests that acid site distribution influences product selectivity. For the catalysts containing 5%, 15%, 25%, and 35% W, the density of medium-strength acid sites (μmol m^{-2}) was determined to be 0.156–0.483, 0.455–1.201, 0.561–1.290, and 0.501–1.121 μmol m^{-2}, respectively. Glycerol conversion does not show a direct correlation with medium acid strength alone. Instead, it appears to follow the trend of total acidity. This observation is consistent with the findings of Talebian-Kiakalaieh *et al.*,[60] who reported that total acidity has a stronger influence on glycerol conversion than individual acid strength levels.

A closer examination of Table 1 and Fig. 9 shows that glycerol conversion increases as total acidity rises within the range of 0.483 to 1.29 μmol m^{-2}. A slight increase in acetaldehyde selectivity is also observed over this range. This trend suggests that total acidity influences overall conversion, while individual reactions, including side reactions, are governed by acid sites of specific strength and nature. In particular, medium-strength acid sites correlate more directly with acrolein formation, which is associated with Brønsted acid sites of intermediate strength. Under the examined reaction conditions, the 25% W–KIT-6 sample, characterized by an elevated medium-strength acid site density per unit surface area (0.561–1.290 μmol m^{-2}), achieves the highest acrolein yield among all tested catalysts. These observations indicate that acid site distribution affects product selectivity in glycerol dehydration. It should be noted that NH_3-TPD provides information on acid strength distribution, whereas pyridine-FTIR distinguishes between Brønsted and Lewis acid sites. These techniques describe different aspects of surface acidity. Although weak acid sites are dominant, they are mainly associated with Lewis acidity and show lower selectivity toward acrolein. These sites may contribute to side reactions leading to by-product formation. In contrast, Brønsted acid sites of medium strength are responsible for acrolein formation. Therefore, even a smaller fraction of Brønsted acid sites can determine the reaction selectivity. This is consistent with the 25 wt% W–KIT-6 catalyst, which shows the highest acrolein yield in correlation with its higher B/(B + L) ratio and increased medium-strength Brønsted acidity.

The relationship between medium acid strength, glycerol conversion, and acrolein yield is presented in Fig. 10. The data show that variations in acidity parameters influence both conversion and selectivity. Catalysts with moderate WO_3 loadings exhibit a favorable balance between medium-strength Brønsted and Lewis acid sites. Acrolein formation is

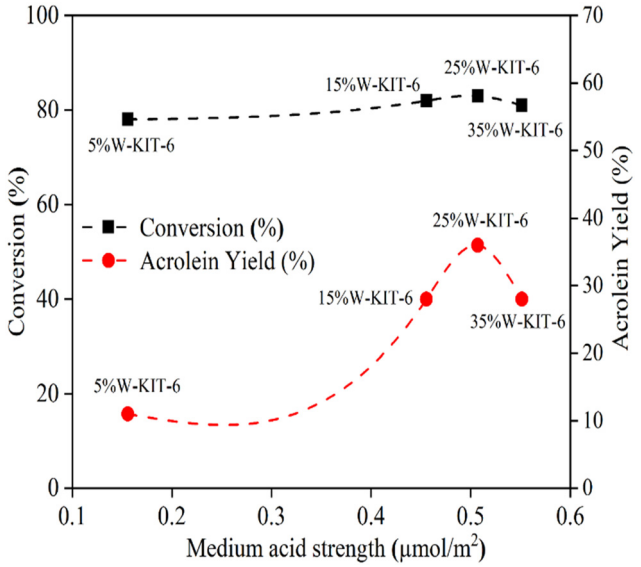

Fig. 10 Relation between the density of medium-strength acid sites, conversion, and acrolein yield.

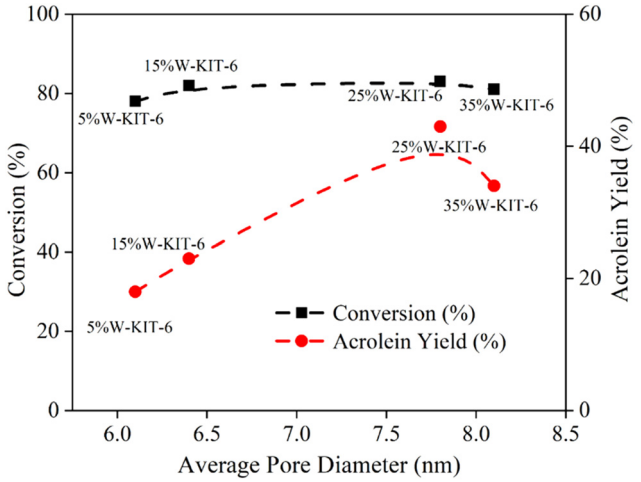

Fig. 11 Relation between the average pore diameter, conversion, and acrolein yield.

primarily associated with Brønsted acid sites of intermediate strength, whereas Lewis acid sites are more closely related to side reactions leading to by-products. Accordingly, a higher proportion of medium-strength Brønsted acid sites relative to Lewis sites favors acrolein formation while limiting excessive by-product formation. These observations suggest that acid site distribution plays a significant role in governing product selectivity in glycerol dehydration.

4.3. Pore size effects on acrolein production

Pore diameter may influence mass transport during glycerol dehydration. Fig. 11 shows that glycerol conversion does not vary significantly with pore size within the studied range. However, acrolein yield exhibits some variation with pore diameter. The catalysts follow the order 7.8 nm > 8.1 nm > 6.4 nm > 6.1 nm in terms of acrolein yield, as summarized in Table 1. Catalysts with pore diameters near or above 8 nm show relatively higher acrolein yields compared to those with smaller pores. This trend suggests that textural properties may influence product selectivity, possibly through differences in reactant accessibility.

Similar observations have been reported for glycerol dehydration over porous materials. Zhang *et al.* and Zhao *et al.*[61,62] reported that restricted pore structures can affect acrolein formation, whereas larger and more open pores may facilitate improved catalytic performance. In the present study, the results indicate that pore size is one of several parameters that contribute to catalytic behavior alongside acidity and WO_3 loading.

Acrolein yield decreases with time on stream for all catalysts. After six hours, the final acrolein yields are 26%, 24%, 16%, and 15% for 35%, 25%, 5%, and 15% W–KIT-6, respectively. The 15% W–KIT-6 catalyst shows the largest relative decline in acrolein yield, corresponding to a decrease of 35%.

In comparison, the 5% W–KIT-6 and 35% W–KIT-6 catalysts exhibit smaller decreases of approximately 7%. These results indicate differences in catalyst stability as a function of W loading.

Despite comparable pore diameters in the 5% and 15% W–KIT-6 catalysts, the 15% W sample exhibits a more pronounced decline in acrolein yield. This difference may be associated with its higher total acidity and increased concentrations of Brønsted and Lewis acid sites. Brønsted acid sites are known to promote acrolein formation, but they have also been linked to coke formation in glycerol dehydration reactions. Although the 25% W–KIT-6 catalyst presents higher Brønsted acidity than the 15% W sample, it shows improved stability under the studied conditions. This observation suggests that catalytic stability depends on multiple factors, including acidity

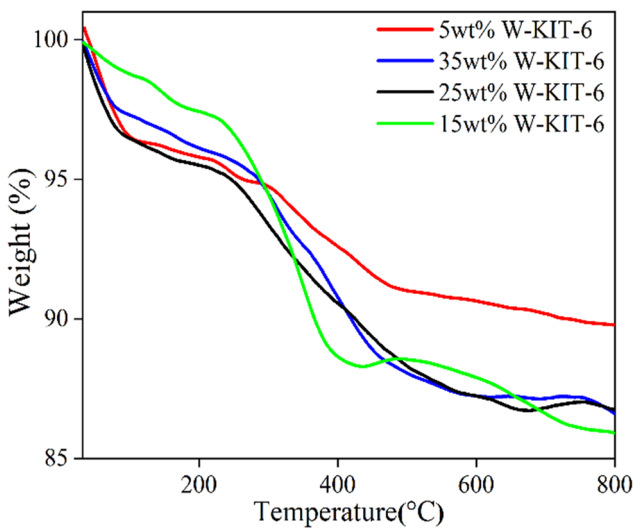

Fig. 12 TGA curves for spent catalysts: 5–35 wt% W–KIT-6.

distribution and textural properties. Smaller pore diameters may influence mass transport and contribute to differences in deactivation behavior. These results indicate that the relationship between acidity and pore size affects long-term catalytic performance. Catalysts with moderate acidity and relatively larger pore diameters show improved stability compared to those with higher acidity and smaller pores within the investigated range.

4.4. Coke control in the WO_3/KIT-6 catalysts

TGA analysis of the spent catalysts is shown in Fig. 12. After six hours on stream, coke contents of 7.7%, 14.5%, 12.3%, and 10% are measured for 5%, 15%, 25%, and 35% W–KIT-6, respectively. No clear linear relationship is observed between coke content and individual parameters such as total acidity, Brønsted acid concentration, or pore diameter, as presented in Fig. 13. The 15% W–KIT-6 catalyst exhibits the highest coke content (14.5%) and also shows the largest decline in acrolein yield. The data further suggest that coke deposition depends on multiple interacting factors rather than a single structural or acidity parameter within the investigated range.

These results indicate that Brønsted acid sites are often associated with coke formation, as reported in the literature.[63] However, the relationship between acidity and coke deposition appears to depend on multiple interacting factors. The 15% W–KIT-6 catalyst, which exhibits relatively high total acidity, shows higher coke formation. This behavior may be related to stronger interactions between reactive intermediates and acid sites. In contrast, the 35% W–KIT-6 catalyst presents lower coke deposition despite comparable acidity levels. This observation suggests that textural properties, including pore diameter, may influence deactivation behavior. Larger pore sizes may facilitate the diffusion of reaction intermediates and reduce their residence time on the catalyst surface. Overall, the data indicate that both acidity distribution and textural characteristics contribute to long-term catalytic stability under the studied conditions.

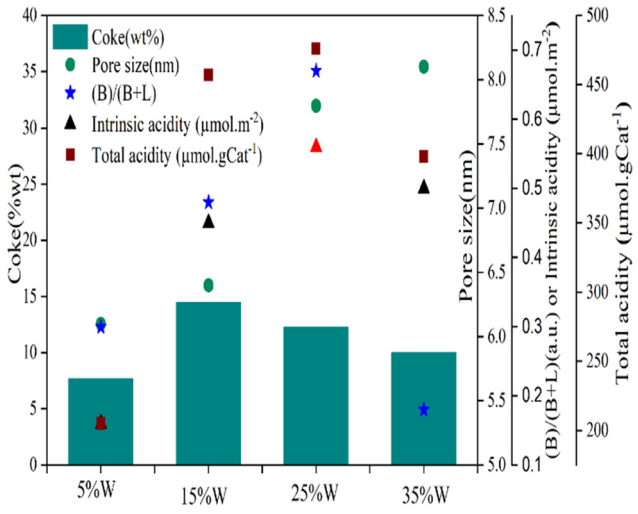

Fig. 13 Relationship between coke (wt%), total acidity (μmol g^{-1}), and pore size (nm).

In addition, the TGA profiles provide insight into the nature of coke species deposited on the catalyst surface. Weight loss at lower temperatures (200–400 °C) is associated with less stable carbon species (soft coke). Weight loss at higher temperatures (above 400 °C) corresponds to more stable carbon deposits (hard coke). These results suggest that coke formation involves carbon species with different thermal stabilities.

This study examines the relationship between coke deposition and catalyst properties under the investigated conditions. The results indicate that acidity and textural characteristics both influence deactivation behavior.

However, the interaction between these parameters requires further clarification. Future work involving detailed mechanistic analysis may provide deeper insight into the roles of acid site distribution and pore accessibility in coke formation. Additional studies under varied reaction conditions could further clarify how catalyst composition affects long-term stability.

Conclusions

In this work, WO_3/KIT-6 catalysts with tungsten oxide loadings between 5 and 35 wt% were prepared using the non-hydrolytic sol–gel method and evaluated for glycerol dehydration to acrolein. The catalysts exhibit mesoporous characteristics and tungsten oxide phases within the investigated loading range. Surface acidity increases with WO_3 loading up to 25 wt%, accompanied by changes in acid site distribution. Among the studied catalysts, 25% W–KIT-6 shows the highest acrolein selectivity (43%) at 83% glycerol conversion. This catalyst presents a relatively high concentration of medium-strength acid sites (204 μmol NH_3 per g), an intrinsic acidity of 0.56 μmol NH_3 per m^2, and a Brønsted/(Brønsted + Lewis) ratio of 0.67. The correlation between acrolein selectivity and medium acid strength suggests that acid site distribution plays an important role in product formation. Textural properties, including the pore diameter in the range of 6–8 nm, also influence catalytic behavior. Catalysts with relatively larger pore diameters show improved stability under the studied conditions. TGA analysis indicates that coke deposition varies with WO_3 loading and acidity, and does not depend on a single parameter alone. The results demonstrate that catalytic performance in glycerol dehydration depends on the combined influence of WO_3 loading, acidity distribution, and textural characteristics within the investigated range.

Author contributions

Busra Kaya: conceptualization, investigation, methodology, data curation, formal analysis, and writing – original draft. Mohammed Alfatih Hamid: investigation, methodology,

formal analysis, writing – original draft, and visualization. Yasar Zengin: investigation, methodology, data curation, formal analysis, and writing – review & editing. Mehtap Safak Boroglu: supervision, resources, validation, and writing – review & editing. Ismail Boz: supervision, funding acquisition, project administration, and review & editing.

Conflicts of interest

There are no conflicts to declare.

Data availability

All data supporting the findings of this study are available within the article and its supplementary information (SI). Additional raw datasets are available from the corresponding author upon reasonable request.

The supplementary information includes additional SEM images of pure KIT-6, XPS analysis (survey, O 1s, W 4f, and Si 2p spectra), and elemental quantification data (Table S1). See DOI: https://doi.org/10.1039/d6re00079g.

Notes and references

1 P. H. P. S. Guedes, R. F. Luz, R. M. Cavalcante and A. F. Young, *Biomass Bioenergy*, 2023, **168**, 106659.
2 B. Kaya, M. A. Hamid, Y. Zengin, M. Safak Boroglu and I. Boz, *Ind. Eng. Chem. Res.*, 2024, **63**, 19486–19497.
3 C. Huang, C. Xu, B. Wang, X. Hu, J. Li, J. Liu, J. Liu and C. Li, *Biomass Bioenergy*, 2018, **119**, 173–178.
4 X. Wang, F. Zhao and L. Huang, *Catalysts*, 2020, **10**, 43.
5 E. Kraleva, R. Palcheva, L. Dimitrov, U. Armbruster, A. Brückner and A. Spojakina, *J. Mater. Sci.*, 2011, **46**, 7160–7168.
6 H. Li, Y. Wang, C. Zhang, Z. Huang, J. Han, X. Nie and F. Wang, *Appl. Catal., B*, 2023, **325**, 122342.
7 A. Tresatayawed, P. Glinrun and B. Jongsomjit, *Int. J. Chem. Eng.*, 2019, **2019**, 4936292.
8 T. Aihara, K. Asazuma, H. Miura and T. Shishido, *RSC Adv.*, 2020, **10**, 37538–37544.
9 N. Le Houx, G. Pourroy, F. Camerel, M. Comet and D. Spitzer, *J. Phys. Chem. C*, 2010, **114**, 155–161.
10 L. M. Bertus, C. Faure, A. Danine, C. Labrugere, G. Campet, A. Rougier and A. Duta, *Mater. Chem. Phys.*, 2013, **140**, 49–59.
11 Y. Zengin, M. A. Hamid, B. Kaya, M. S. Boroglu and I. Boz, *Mater. Today Commun.*, 2025, **47**, 113079.
12 C. Chacón, M. Rodríguez-Pérez, G. Oskam and G. Rodríguez-Gattorno, *J. Mater. Sci.: Mater. Electron.*, 2015, **26**, 5526–5531.
13 V. Smeets, A. Styskalik and D. P. Debecker, *J. Sol-Gel Sci. Technol.*, 2021, **97**, 505–522.
14 S. Zhao, Y. Shen, P. Zhou, G. Li, C. Han, D. Wei, X. Zhong, Y. Zhang and Y. Ao, *Nanomaterials*, 2019, **9**, 8.
15 A. Styskalik, D. Skoda, C. E. Barnes and J. Pinkas, *Catalysts*, 2017, **7**, 168.
16 S. Maksasithorn, P. Praserthdam, K. Suriye, M. Devillers and D. P. Debecker, *Appl. Catal., A*, 2014, **488**, 200–207.
17 L. Nadji, A. Massó, D. Delgado, R. Issaadi, E. Rodriguez-Aguado, E. Rodriguez-Castellón and J. M. López Nieto, *RSC Adv.*, 2018, **8**, 13344–13352.
18 I. Boz, M. S. Boroglu, Y. Zengin and B. Kaya, *Inorg. Chem. Commun.*, 2023, **147**, 110240.
19 J. A. Cecilia, C. García-Sancho, J. M. Mérida-Robles, J. Santamaría González, R. Moreno-Tost and P. Maireles-Torres, *Appl. Catal., A*, 2016, **516**, 30–40.
20 Y. Zengin, B. Kaya, M. Safak Boroglu and I. Boz, *Ind. Eng. Chem. Res.*, 2023, **62**, 1852–1864.
21 M. Battisti, N. Hollik, A. Meise, M. Heggen, C. Mebrahtu and R. Palkovits, *Catal. Sci. Technol.*, 2026, **16**, 2321–2330.
22 S. H. Chai, L. Z. Tao, B. Yan, J. C. Vedrine and B. Q. Xu, *RSC Adv.*, 2014, **4**, 4619–4630.
23 N. V. Vlasenko, G. R. Kosmambetova, E. V. Senchylo, K. Peter, K. Veltruská and P. E. Strizhak, *ChemSusChem*, 2025, **18**, 1–9.
24 J. Sun, Q. Kan, Z. Li, G. Yu, H. Liu, X. Yang, Q. Huo and J. Guan, *RSC Adv.*, 2014, **4**, 2310–2317.
25 A. Ramanathan, R. Maheswari, D. H. Barich and B. Subramaniam, *Microporous Mesoporous Mater.*, 2014, **190**, 240–247.
26 H. Oveisi, C. Anand, A. Mano, S. S. Al-Deyab, P. Kalita, A. Beitollahi and A. Vinu, *J. Mater. Chem.*, 2010, **20**, 10120–10129.
27 D. Le, N. Chaidherasuwet, A. Rueangthaweep, C. Kulsing and N. Hinchiranan, *Catal. Today*, 2023, **407**, 260–273.
28 N. La Salvia, D. Delgado, L. Ruiz-Rodríguez, L. Nadji, A. Massó and J. M. L. Nieto, *Catal. Today*, 2017, **296**, 2–9.
29 R. Kishor and A. K. Ghoshal, *Microporous Mesoporous Mater.*, 2017, **242**, 127–135.
30 H. Zhu, A. Ramanathan, J.-F. Wu and B. Subramaniam, *ACS Catal.*, 2018, **8**, 4848–4859.
31 R. Guillet-Nicolas, R. Ahmad, K. A. Cychosz, F. Kleitz and M. Thommes, *New J. Chem.*, 2016, **40**, 4351–4360.
32 A. Duan, T. Li, Z. Zhao, B. Liu, X. Zhou, G. Jiang, J. Liu, Y. Wei and H. Pan, *Appl. Catal., B*, 2015, **165**, 763–773.
33 Y. Lu, J. Zhang, F. Wang, X. Chen, Z. Feng and C. Li, *ACS Appl. Energy Mater.*, 2018, **1**, 2067–2077.
34 D. D. Eslek Koyuncu, I. Tug, N. Oktar and K. Murtezaoglu, *ChemPlusChem*, 2025, **90**, e202400665.
35 C.-I. Ahn, Y. Kwak, A.-R. Kim, M. Jang, A. Badakhsh, J. Cha, Y. Kim, Y. S. Jo, H. Jeong, S. H. Choi, S. W. Nam, C. W. Yoon and H. Sohn, *Appl. Catal., B*, 2022, **307**, 121169.
36 Y. Li, Y. Chen, L. Li, J. Gu, W. Zhao, L. Li and J. Shi, *Appl. Catal., A*, 2009, **366**, 57–64.
37 A. Boulaoued, I. Fechete, B. Donnio, M. Bernard, P. Turek and F. Garin, *Microporous Mesoporous Mater.*, 2012, **155**, 131–142.
38 P. Shukla, H. Sun, S. Wang, H. M. Ang and M. O. Tadé, *Catal. Today*, 2011, **175**, 380–385.
39 M. A. Hamid, E. Kutbay and S. Suzer, *Anal. Methods*, 2026, **18**, 3056–3064.
40 X. Q. Wang, H. L. Ge, H. X. Jin and Y. J. Cui, *Microporous Mesoporous Mater.*, 2005, **86**, 335–340.

41 Y. H. Guo, C. Xia and B. S. Liu, *Chem. Eng. J.*, 2014, **237**, 421–429.
42 F. R. D. Fernandes, F. G. H. S. Pinto, E. L. F. Lima, L. D. Souza, V. P. S. Caldeira and A. G. D. Santos, *Appl. Sci.*, 2018, **8**, 725.
43 W. Wang, R. Qi, W. Shan, X. Wang, Q. Jia, J. Zhao, C. Zhang and H. Ru, *Microporous Mesoporous Mater.*, 2014, **194**, 167–173.
44 T.-W. Kim, F. Kleitz, B. Paul and R. Ryoo, *J. Am. Chem. Soc.*, 2005, **127**, 7601–7610.
45 A. Wawrzyńczak, S. Jarmolińska and I. Nowak, *Catal. Today*, 2022, **397–399**, 526–539.
46 D.-H. Choi and R. Ryoo, *J. Mater. Chem.*, 2010, **20**, 5544–5550.
47 J. Datka, A. M. Turek, J. M. Jehng and I. E. Wachs, *J. Catal.*, 1992, **135**, 186–199.
48 H. Gan, X. Zhao, B. Song, L. Guo, R. Zhang, C. Chen, J. Chen, W. Zhu and Z. Hou, *Chin. J. Catal.*, 2014, **35**, 1148–1156.
49 N. Poovarawan, K. Suriye, J. Panpranot, W. Limsangkass, F. J. Santos Cadete Aires and P. Praserthdam, *Catal. Lett.*, 2015, **145**, 1868–1875.
50 A. B. Kulal, M. K. Dongare and S. B. Umbarkar, *Appl. Catal., B*, 2016, **182**, 142–152.
51 F. Di Gregorio, N. Keller and V. Keller, *J. Catal.*, 2008, **256**, 159–171.
52 V. V. Brei, O. V. Melezhyk, S. V. Prudius, G. M. Tel'Biz and O. I. Oranska, *Adsorpt. Sci. Technol.*, 2005, **23**, 109–114.
53 J.-F. Wu, A. Ramanathan, W. K. Snavely, H. Zhu, A. Rokicki and B. Subramaniam, *Appl. Catal., A*, 2016, **528**, 142–149.
54 H. Sun, F. Song, C. Zhou, X. Wan, Y. Jin, Y. Dai, J. Zheng, S. Yao and Y. Yang, *Catal. Commun.*, 2021, **149**, 106254.
55 D. P. Debecker and P. H. Mutin, *Chem. Soc. Rev.*, 2012, **41**, 3624–3650.
56 J. Kaur, K. Anand, K. Anand and R. C. Singh, *J. Mater. Sci.*, 2018, **53**, 12894–12907.
57 R. Aghaei and A. Eshaghi, *J. Alloys Compd.*, 2017, **699**, 112–118.
58 J. F. Moulder, W. F. Stickle, P. E. Sobol and K. D. Bomben, *Handbook of X-ray Photoelectron Spectroscopy*, Perkin-Elmer Corporation, 1992.
59 E. Ciftyurek, B. Šmíd, Z. Li, V. Matolín and K. Schierbaum, *Sensors*, 2019, **19**, 4737.
60 A. Talebian-Kiakalaieh and N. A. S. Amin, *Catal. Today*, 2015, **256**, 315–324.
61 H. Zhang, Z. Hu, L. Huang, H. Zhang, K. Song, L. Wang, Z. Shi, J. Ma, Y. Zhuang and W. Shen, *ACS Catal.*, 2015, **5**, 2548–2558.
62 S. Zhao, W. D. Wang, L. Wang, W. Wang and J. Huang, *J. Catal.*, 2020, **389**, 166–175.
63 B. Liu, D. Slocombe, M. AlKinany, H. AlMegren, J. Wang, J. Arden, A. Vai, S. Gonzalez-Cortes, T. Xiao, V. Kuznetsov and P. P. Edwards, *Appl. Petrochem. Res.*, 2016, **6**, 209–215.